IMPROVEMENTS IN NONCONVECTIVE AVIATION TURBULENCE PREDICTION FOR THE WORLD AREA FORECAST SYSTEM

Jung-Hoon Kim, Robert Sharman, Matt Strahan, Joshua W. Scheck, Claire Bartholomew, Jacob C. H. Cheung, Piers Buchanan, and Nigel Gait

A multidiagnostic-based en route nonconvective turbulence forecasting algorithm has been developed to provide better predictions of clear-air and mountain-wave turbulence for use in global strategic flight planning.

In-flight bumpiness due to unexpected turbulence encounters can be the most stressful and inconvenient experience for people on board commercial aircraft. It can be more hazardous at cruising altitudes where flight crew and passengers are likely to be unbuckled, which may lead to serious inflight injuries as well as structural damage and premature aging of the airframe and flight/service delays (Sharman and Lane 2016). Because of the rapid and continuing increase in air traffic, and perhaps impacts from global warming, there is some evidence that the number of turbulence encounters has been increasing (Jaeger and Sprenger 2007; Wolff and Sharman 2008; Kim and Chun 2011) and are expected to continue to rise in the future (e.g., Williams and Joshi 2013; Williams 2017; Storer et al. 2017).

Motivation. The World Area Forecast Centers (WAFCs) were established in 1982 by the International Civil Aviation Organization (ICAO) in conjunction with the World Meteorological Organization (WMO). Two WAFCs, one in Washington, D.C., and another in London, United Kingdom, provide 6-hourly digital forecasts of significant en route weather on a global basis. These forecasts include information on wind, temperature, turbulence, convection, and icing to aviation users across the world (Gill 2014).

Automated and gridded weather prediction information provided by the WAFCs' World Area Forecast System (WAFS) can be directly used by airlines for strategic flight planning including the avoidance of aviation weather hazards, particularly for long-haul flights (ICAO 2012). Users can access the WAFS data via the Secure Aviation Data Information Service (SADIS) from WAFC London and/or the WAFS Internet File Service (WIFS) from WAFC Washington. The ICAO Global Air Navigation Plan (GANP) is a comprehensive planning tool supporting a harmonized global air navigation system. This planning approach uses the Aviation System Block Upgrade

Table 1. Requirements for the WAFS upgrade in support of the ICAO's ASBU plans (WMO–ICAO 2014).		
Blocks	**Requirements**	**Resolution**
Overarching requirements	Continue to provide gridded diagnostics for turbulence, icing, and convection	3 hourly from T + 6 to T + 36 Every 6 h (0000, 0600, 1200, and 1800 UTC) 1.25° × 1.25° grid
ASBU 0 (~2018)	Provide improved forecast algorithms to replace potentials with intensities (viz., EDR for turbulence) Provide global and regional verification of WAFS products	3 hourly from T + 6 to T + 36 Every 6 h 0.5° × 0.5° grid
ASBU 1 (2019–24)	Provide calibrated probabilistic forecasts for turbulence, icing, and convection Implement finer grid resolution for WAFS Implement turbulence type forecasts (e.g., CIT, CAT, and MWT) Make available WAFS data via the System Wide Information Management (SWIM)	3 hourly from T + 6 to T + 36 Every 6 h 0.25° × 0.25° grid
ASBU 2 (2025–30)	Provide increased en route weather dataset suitable for integration into flight planning and decision support system	3 hourly from T + 6 to T + 36 Every 3 h 0.25° × 0.25° grid
ASBU 3 (2030~)	Provide fully integrated multimember ensemble hazard forecasts Implement high spatial and temporal resolution models Provide fully automated gridded and significant weather forecast (SIGWX)	1 hourly from T + 6 to T + 72 Every 1 h 0.1° × 0.1° grid 1,000 ft vertical

(ASBU) to match the capabilities of modern aircraft toward an improved and interoperable future air traffic management (ATM) system that is safe, cost effective, and environmentally friendly (Civil Air Navigation Services Organization 2014). The ASBU comprises 6-yr blocks of technical advances by 2018 for block 0, 2019–24 for block 1, 2025–30 for block 2, and beyond 2030 for block 3. For aviation weather, ICAO requested that the WAFS upgrades are in line with the ASBU periods. Detailed information on the WAFS upgrades is described in Table 1.

AFFILIATIONS: Kim—School of Earth and Environmental Sciences (SEES), Seoul National University (SNU), Seoul, South Korea; Sharman—National Center for Atmospheric Research, Boulder, Colorado; Strahan and Scheck—NOAA/Aviation Weather Center, Kansas City, Missouri; Bartholomew, Cheung, Buchanan, and Gait*—Met Office, Exeter, United Kingdom
* Retired.
CORRESPONDING AUTHOR: Prof. Jung-Hoon Kim, jhkim99@snu.ac.kr

The abstract for this article can be found in this issue, following the table of contents.
DOI:10.1175/BAMS-D-17-0117.1

In final form 14 April 2018

For turbulence, the current gridded WAFS forecasts use global numerical weather prediction (NWP) model output to estimate an uncalibrated turbulence potential on a 1.25° × 1.25° global domain based on a single empirical turbulence diagnostic, the Ellrod index (Ellrod and Knapp 1992), which depends on vertical wind shear and total deformation. In accordance with the ASBU plan in Table 1, the ICAO and WMO have requested an upgrade of the current WAFS turbulence product to provide a calibrated severity atmospheric turbulence metric, namely, energy dissipation rate (EDR) to the 1/3 power ($m^{2/3}\ s^{-1}$) for multiple sources of turbulence, and also produce probabilistic forecasts with better spatial and temporal resolutions (WMO–ICAO 2014).

Background. Atmospheric turbulence relevant to cruising aircraft in the upper troposphere–lower stratosphere (UTLS) is categorized into three different types based on their locations and generation mechanisms: clear-air turbulence (CAT), mountain-wave turbulence (MWT), and convectively induced turbulence (CIT; Fig. 1; e.g., Lester 1994; Wolff and Sharman 2008; Kim and Chun 2011; Sharman and Lane 2016).

CAT is frequent near upper-level jets/frontal systems. Kelvin–Helmholtz instability (KHI) due to the strong vertical wind shear above and below the jet core is one of the well-known sources

for CAT (e.g., Dutton and Panofsky 1970) and is related to small values of the gradient Richardson number (Ri; a nondimensional ratio between vertical shear and stability). Upper-level frontogenesis (e.g., Ellrod and Knapp 1992) along with tropopause folding (e.g., Kim and Chun 2010) plays an important role in inducing CAT near jet streams. Inertia–gravity waves (IGWs) generated by unbalanced flow locally enhance shear and reduce stability and can trigger KHI near jet streams (e.g., Lane et al. 2004; Koch et al. 2005; Zhang 2004). CAT is also associated with strong ageostrophic flow, inertial instability, and spontaneous emission of IGWs, especially on the anticyclonic shear side and in strong curvature regions of midlatitude jet streaks (e.g., Knox 1997).

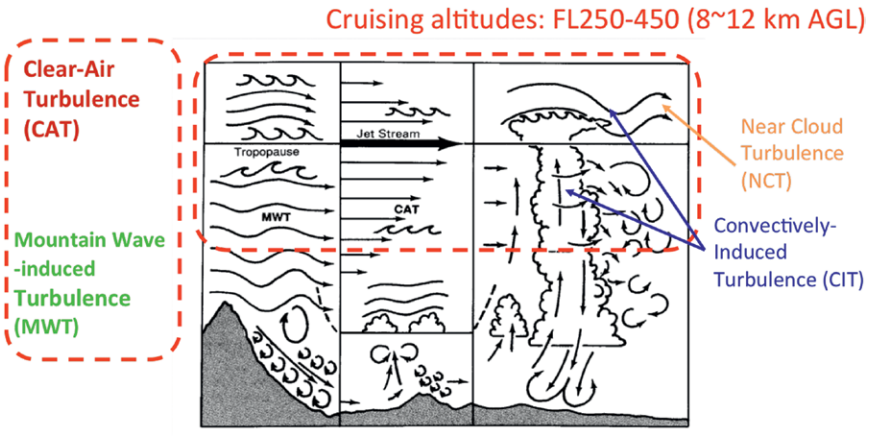

Fig. 1. Aviation turbulence classifications, representing a pictorial summary of turbulence phenomena that may occur in each turbulence classification [adapted from Lester (1994); Jeppesen Sanderson, Inc.].

Vertically propagating mountain waves can form when near-surface wind passes over mountain regions (Fig. 1). The characteristics of these mountain waves such as wave amplitude and wavelength are highly dependent upon the topography, low-level flow, and atmospheric vertical structure. As the wave propagates upward, its amplitude grows because of the decrease in air density, which may cause wave saturation, breaking, and localized mixing (e.g., Doyle et al. 2005; Clark and Peltier 1984). Wave propagation and saturation conditions are strongly related to background wind and stability profiles. For example, wave breaking is frequent above the jet stream core and near the tropopause. Also, stationary mountain waves can break down near critical levels via a nonlinear effect where wave phase speed is equal to the background wind projected onto the wave vector (e.g., Lilly 1978; Lane et al. 2009; Sharman et al. 2012a,b). In the process of wave breaking, horizontal vortex tubes (Clark et al. 2000) and secondary gravity waves (Kim and Chun 2010; Lane and Sharman 2006) can also contribute to the MWT.

CIT is normally categorized into in-cloud and out-of-cloud CIT, depending on the location (Fig. 1). Although aircraft use visible cloud boundaries or regions of onboard radar echoes to avoid in-cloud CIT, out-of-cloud CIT [especially far away from convection; i.e., near-cloud turbulence (NCT; Lane et al. 2012; Lane 2016)] is still challenging to predict using current NWP models. Previous studies have shown that NCT is associated with various generation mechanisms, such as disturbances due to the convective overshooting tops, convectively induced gravity waves and breaking (e.g., Lane et al. 2012; Lane 2016; Kim and Chun 2012), and thermal-shear stability within a near-neutral layer of cirrus anvil with radial cirrus bands (e.g., Sharman and Lane 2016; Kim et al. 2014). These mechanisms are challenging to capture in current NWP models. However, CIT forecasting is beyond the scope of this paper because it is difficult to forecast the exact timing and location of convective clouds at the current global NWP model resolution unless it is embedded along a large-scale forced frontal system.

En route turbulence forecasting. Atmospheric turbulence in the UTLS directly affecting cruising aircraft has horizontal eddy sizes of a few hundred meters to a few kilometers. This is much smaller than the grid spacing of the current (and near-future version of) global NWP models. However, because the energy of the large-scale disturbances cascades down to smaller scales (e.g., Cho and Lindborg 2001), aircraft-scale turbulence can be logically predicted using NWP model–based turbulence diagnostics formulated based on the aforementioned turbulence generation mechanisms (e.g., Gill 2014; Kim et al. 2011, 2015; Kim and Chun 2016; Sharman et al. 2006; Sharman and Pearson 2017).

For operations in the United States, the Graphical Turbulence Guidance (GTG; Sharman and Pearson 2017) is developed by the National Center for Atmospheric Research (NCAR) and is publicly available on the web page of the National Oceanic and Atmospheric Administration (NOAA)/Aviation Weather

Center (www.aviationweather.gov/turbulence) with the following features:

1) multiple pieces of information for both CAT and MWT,
2) calibrated turbulence severity fields in terms of EDR that is the ICAO standard for turbulence measurement,
3) standalone algorithms that are applicable to any global NWP model with proper tunings applied, and
4) capability of providing probabilistic forecasts based on calibrated EDR thresholds and treating the diagnostics as an ensemble,

Although GTG is not intended to predict turbulence associated with convection and thunderstorms (CIT or NCT), it may nevertheless give some guidance of possible CIT or NCT if the areas of thunderstorms are properly forecasted by the underlying NWP model. For instance, CIT or NCT can be detectable along a surface front driven mainly by large-scale forcing mechanisms that are resolved by the current resolution of the NWP model. For the WAFS block 0 and 1 upgrades in Table 1, the NOAA/Aviation Weather Center (WAFC Washington) has been collaborating with the Met Office in the United Kingdom (WAFC London) and NCAR to expand the current domestic operational GTG algorithm to the global domain.

This article is intended for the global aviation user community as well as the broader meteorological community to enhance awareness of the WAFS in general and the turbulence upgrade in particular. The emphasis in this paper will be on the global en route turbulence forecasting component of the next-generation WAFS using global NWP model outputs. The second section describes the detailed procedures of the global GTG (G-GTG) for deterministic and probabilistic EDR forecasts on a 0.5° × 0.5° domain. In the third section, objective evaluations of the G-GTG using global in situ EDR measurements will be examined. A summary and future plans for the deterministic and probabilistic EDR forecasts will be provided in the fourth section.

GLOBAL GRAPHICAL TURBULENCE GUIDANCE. In this study, the GTG, version 3 (Sharman and Pearson 2017), is expanded to the global domain by using NOAA's Global Forecast System (GFS; Sela 2010) and the Met Office's Unified Model (UM; Walters et al. 2017) on a 0.5° × 0.5° domain with three sequential procedures as shown in the schematic chart of Fig. 2. It is noted that the native grids of underlying GFS (T574; ~24 km) and UM (T764; ~17 km) NWP models are at higher resolutions than the 0.5° × 0.5° domain used in this study.

Computing individual CAT and MWT diagnostics. The 15 CAT diagnostics used in this study are selected from the suite of the GTG, version 3, component diagnostics that have relatively higher skill scores than others when verified against a long period of upper-level in situ EDR observation data over the conterminous United States (CONUS) as well as outside the CONUS (Sharman and Pearson 2017). Details of the in situ EDR data will be described in the "Objective evaluations" section. For MWT forecasts, Sharman and Pearson (2017) described 14 MWT diagnostics based on combining a 2D surface mountain-wave parameter (mws) with conventional 3D CAT diagnostics. This method is based on the theoretical understanding of the generation, propagation, and saturation of a hydrostatic large-amplitude mountain wave. They tested the 14 MWT diagnostics over the CONUS and evaluated them against a 1-yr period of observed MWT pilot reports (PIREPs). The 14 MWT diagnostics showed good forecasting skill against PIREPs data and were better than the single-column model-based orographic gravity wave drag (OGWD) parameterization scheme (Palmer et al. 1986). In this study, we used 15 MWT diagnostics including these 14 MWT diagnostics (MWT1–14) as well as the OGWD method. A list of the 15 CAT and 15 MWT diagnostics can be found in the appendix.

Figure 3 shows an example snapshot of three CAT (Ellrod3, |DIV|/Ri, and RTKE) and three MWT diagnostics (MWT3, MWT5, and MWT12) at the 300-hPa level, derived from an 18-h forecast based on GFS model output valid at 1800 UTC 6 January 2016. Note that the shadings of each diagnostic have different units and scales. In Fig. 3 (left), higher potentials of CAT are located near the North Atlantic Ocean, northwestern Africa, East Asia, and the southern

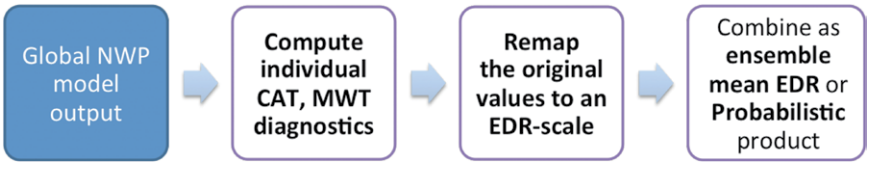

Fig. 2. Schematic chart for the G-GTG that provides either a deterministic ensemble mean of energy dissipation rate to the 1/3 power (EDR) or a probabilistic product, computed from the individual component diagnostics for CAT and MWT based on global NWP model output.

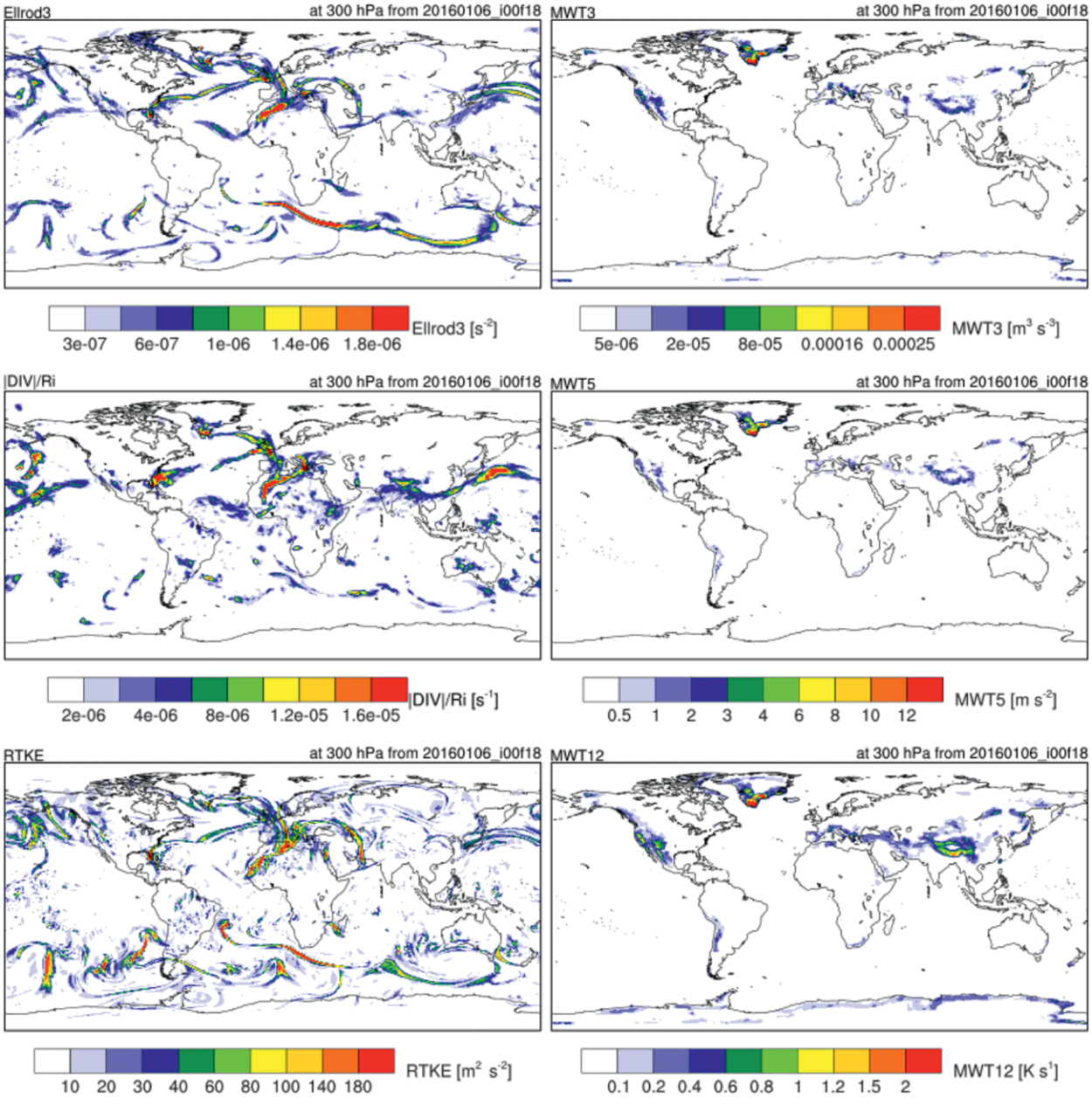

Fig. 3. Snapshot of three CAT [(top left) Ellrod3, (middle left) |DIV|/Ri, and (bottom left) RTKE] and MWT diagnostics [(top right) MWT3, (middle right) MWT5, and (bottom right) MWT12] at the 300-hPa level in the G-GTG for the WAFS upgrade, derived from the 18-h forecast of the GFS model outputs on a 0.5° × 0.5° domain valid at 1800 UTC 6 Jan 2016.

Indian Ocean along the midlatitude jet streams. In Fig. 3 (right), higher potentials of MWT are over southern Greenland, the southwestern Rockies, and the Himalayas. The predicted high potential over the North Atlantic Ocean and southern Greenland are consistent with actual turbulence reports (more detail will be provided in Fig. 10).

Remapping to EDR scale. Once the individual diagnostics within G-GTG are computed from the NWP model output, the next step is to remap them to an EDR scale. This is necessary because the individual turbulence diagnostics have different numerical units and magnitudes that need to be normalized to a common scale before combining in the final step. Here, we use the EDR scale, since EDR is a physically based intensity (severity) metric of atmospheric turbulent eddies in the UTLS affecting aircraft. There are also three advantages of using EDR:

1) It is independent of aircraft size or type and can be translated to the intensity of the turbulence felt by different aircraft using aircraft performance data (e.g., Sharman et al. 2014; Sharman and Pearson 2017).
2) It is the official ICAO standard for turbulence reports from the commercial aircraft (ICAO 2001).
3) EDR forecasts are more useful for consistent and direct comparisons with automated in situ EDR observations from aircraft and for verification purposes (e.g., Sharman et al. 2006, 2014; Kim et al. 2015; Sharman and Pearson 2017).

The conversion methodology suggested by Sharman and Pearson (2017) uses the probability density functions (PDFs) of the individual turbulence diagnostics from the forecast data. Raw turbulence potential values are remapped to EDR by assuming that the predicted turbulence diagnostics follow a lognormal distribution. Several previous field campaign experiments have shown that the observed turbulence in the UTLS does follow a lognormal distribution (e.g., Cho and Lindborg 2001; Nastrom and Gage 1985). In this study, PDFs for the 15 CAT and 15 MWT diagnostics are calculated using a 6-month (October 2015–March 2016) period of 18-h GFS forecasts issued at 0000 UTC. Figure 4 shows example PDFs obtained for three CAT (Ellrod3, |DIV|/Ri, and RTKE) and three MWT (MWT3, MWT5, and MWT12) diagnostics.

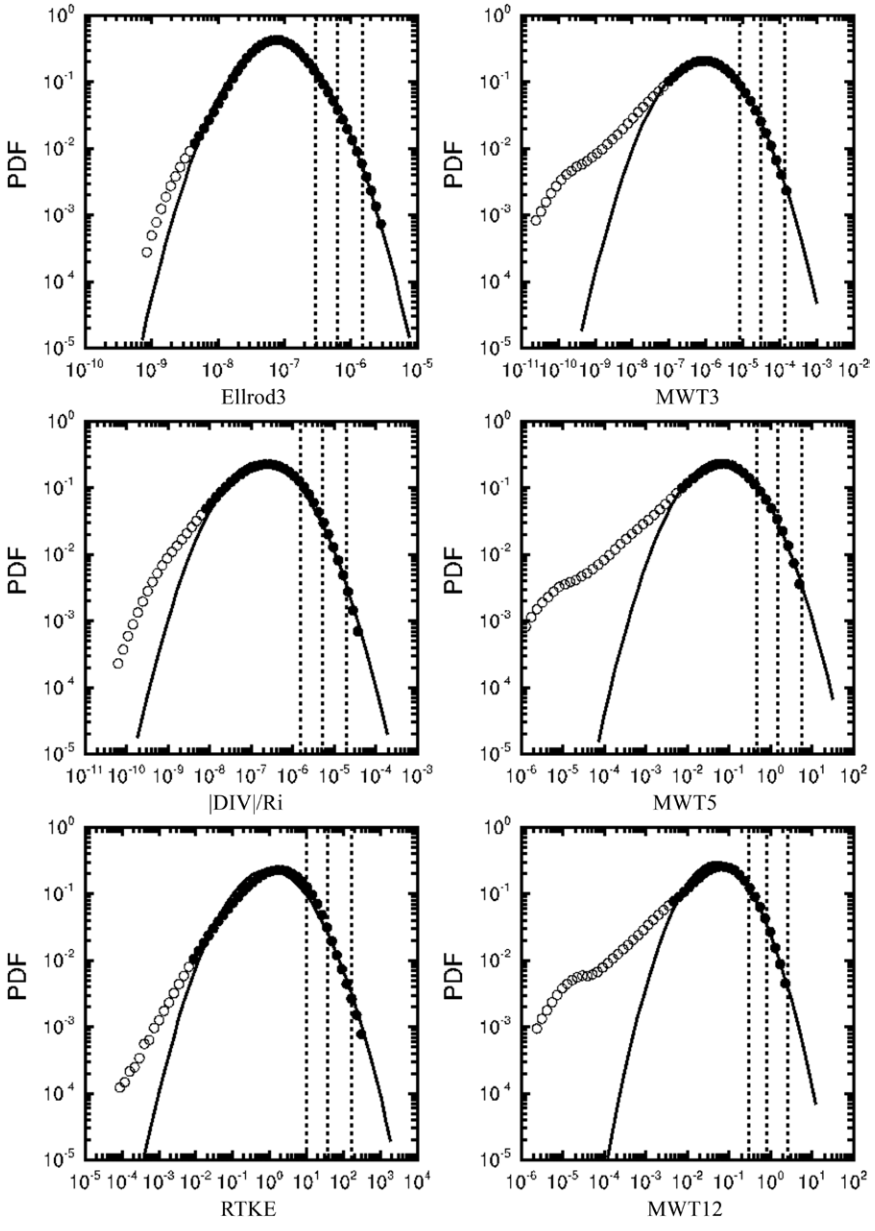

Fig. 4. Example PDFs for three CAT (Ellrod3, |DIV|/Ri, and RTKE) and three MWT (MWT3, MWT5, and MWT12) indices, derived from 6-month period (Oct 2016–Mar 2017) of the 18-h forecast of the GFS model outputs issued at 0000 UTC every day. Relatively higher values of the bins (filled circles) are used for the best-fit function (black solid curve) of the lognormal distribution. Vertical dashed lines show the raw values corresponding to 0.15, 0.22, and 0.34 EDR ($m^{2/3}$ s^{-1}).

In Fig. 4, the circles indicate the raw binned diagnostic values, and the solid curve shows the lognormal fit. The vertical dashed lines from left to right indicate the raw values of the diagnostics corresponding to 0.15, 0.22, and 0.34 EDR ($m^{2/3}$ s^{-1}) values, which are considered as light, moderate, and severe intensities of turbulence for midsize aircraft (Sharman et al. 2014). Note that although the rightmost vertical dashed line for 0.34 EDR falls inside the histogram, the relative frequency of this value is very small (less than 0.01%), which is consistent with the

PDFs for observed in situ EDR data (e.g., Sharman et al. 2014). For these operationally relevant EDR values, all diagnostics shown are fit very well by the assumed lognormal distribution. Figure 5 shows an example snapshot for the converted EDR scale of the same three CAT and MWT diagnostics as in Fig. 3. A comparison with Fig. 3 shows consistent features of each diagnostic.

Deterministic EDR forecast. Once the CAT and MWT diagnostics are calculated and converted into EDR, we combine them using a simple averaging,

$$\mathrm{GTG}(x,y,z)=\left[\sum_{i=1}^{N}\mathrm{EDR}(x,y,z)_i\right]/N,$$

where N is the number of CAT or MWT diagnostics (indicated by subscript i). We believe this multidiagnostic approach can be termed an ensemble method, and therefore, the deterministic G-GTG combination is referred to as the "ensemble mean" of the individual diagnostics, because as shown in Fig. 4, individual CAT and MWT diagnostics are very carefully tuned and converted to an EDR scale in line with climatological EDR observations so that the calibrated individual CAT and MWT diagnostics are equally and randomly distributed well in the model field regardless of their performance skills.

In all events, the maximum gridpoint-by-gridpoint EDR value of the CAT and MWT ensemble mean products provides the final deterministic EDR forecast. Figure 6 shows an example snapshot for the G-GTG EDR forecast based on the GFS model output. In the CAT forecast (upper panel in Fig. 6), higher EDR values occur along the midlatitude jet stream over the North Atlantic Ocean and northwestern Pacific Ocean in the Northern Hemisphere and the southern Indian Ocean in the Southern Hemisphere. It also has a higher EDR forecast near northwestern Africa, which seems to be related to the convergence of the polar jet and

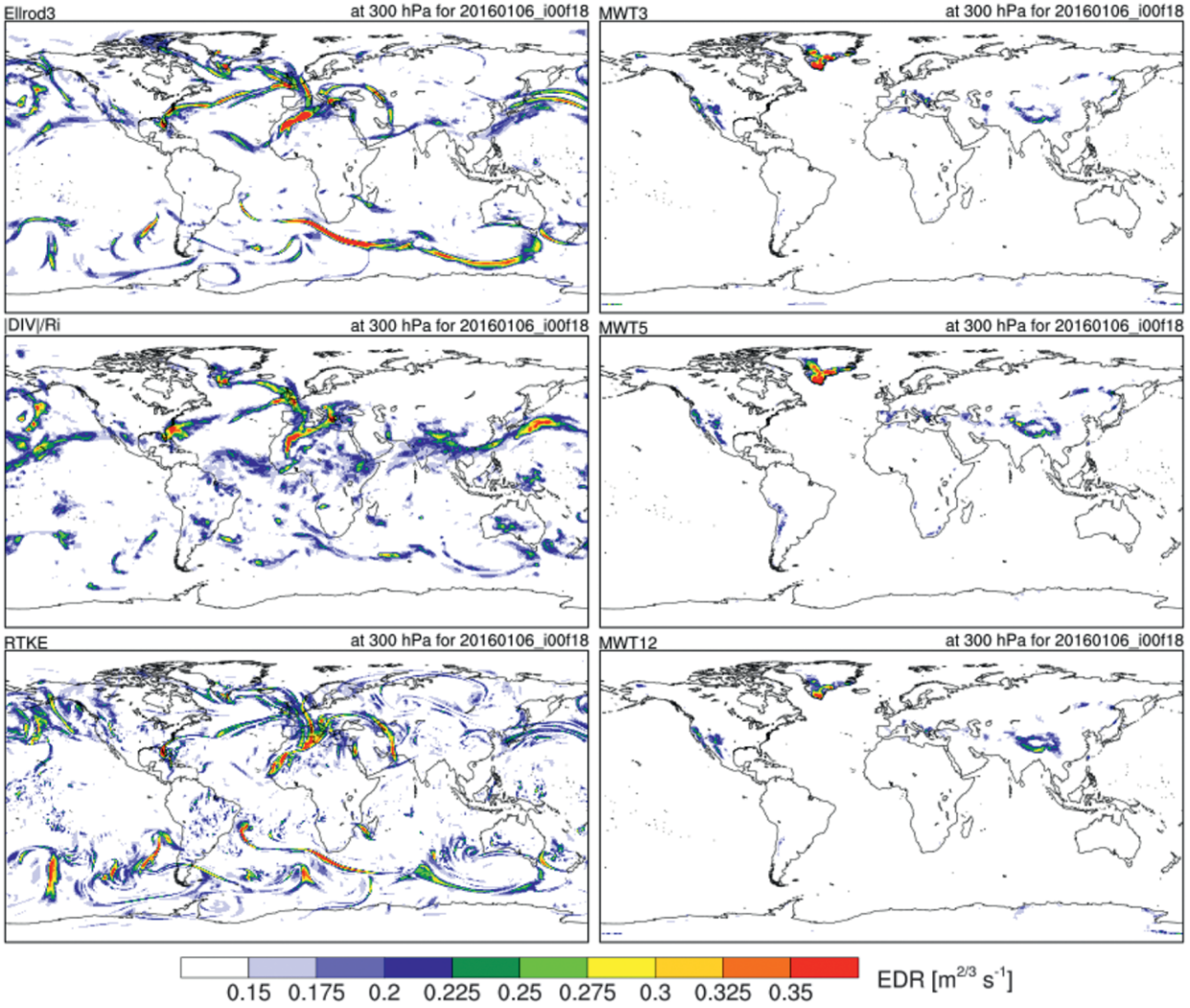

Fig. 5. As in Fig. 3, but for three CAT and MWT diagnostics remapped to the EDR scale.

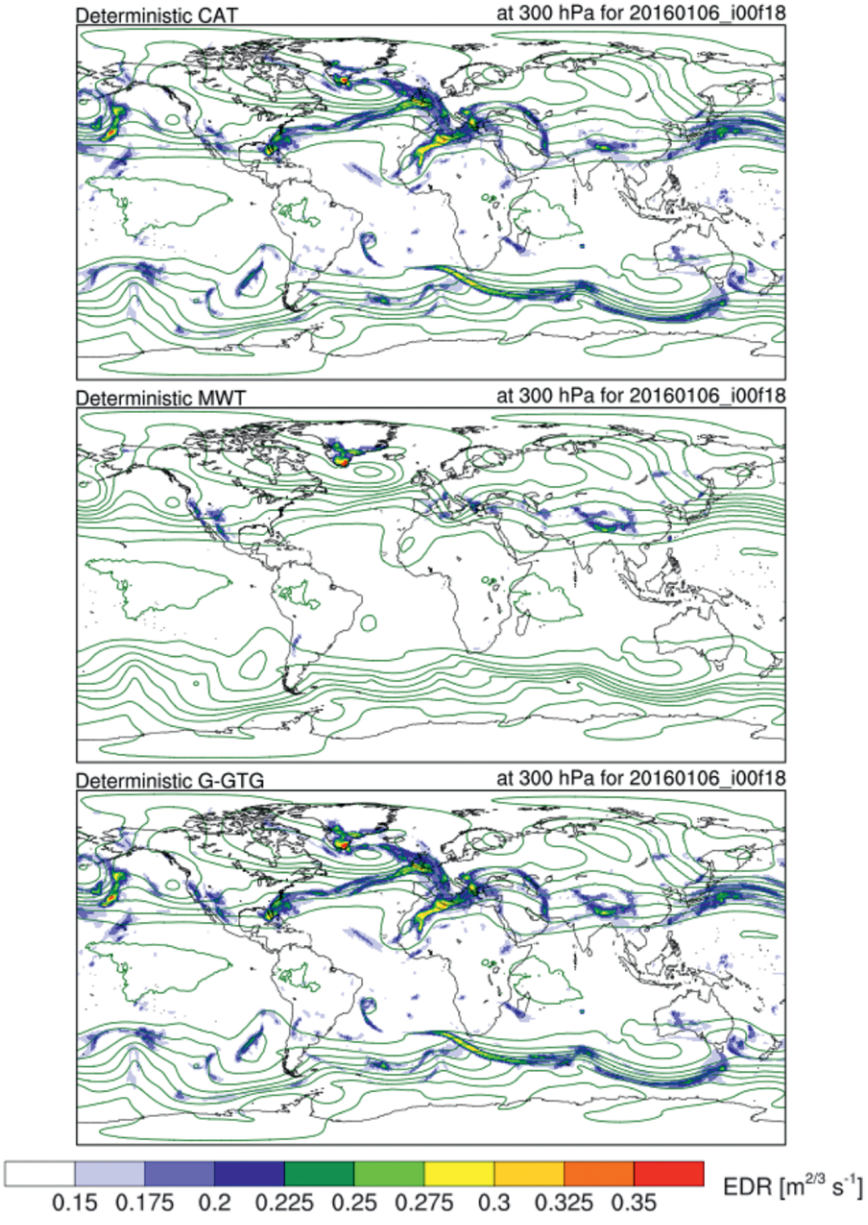

Fig. 6. A snapshot of the deterministic (top) CAT, (middle) MWT, and (bottom) max G-GTG forecasts combined by 15 CAT and 15 MWT individual diagnostics with geopotential height (contour with 160-gpm interval) at 300 hPa, derived from 18-h forecast of the GFS model output on a 0.5° × 0.5° horizontal-resolution domain valid at 1800 UTC 6 Jan 2016. Information about the detailed conversion method to EDR scale and combining diagnostics is in the text.

subtropical jet. In the MWT forecast (middle panel in Fig. 6), higher EDR values are over the southern tip of Greenland and the Himalayas. Finally, the deterministic G-GTG forecast (bottom panel in Fig. 6) is taken from the maximum of those EDR values from the CAT and MWT forecasts. In particular, higher EDR forecasts over the North Atlantic Ocean and southern Greenland agree well with observations, which will be discussed further in the "Blending of GFS-based G-GTG and UM-based G-GTG" section.

Probabilistic EDR forecast. Given that the underlying NWP model and the turbulence diagnostics are not perfect, the uncertainty in the forecasts should be taken into account (e.g., Gill and Buchanan 2014). To quantify this uncertainty, NWP ensemble forecasts using the numerically orthogonal perturbations for initial conditions are developed (e.g., Buizza et al. 1999). However, global NWP ensemble forecasts, by targeting long-term (1–2 week) forecasts, are less dispersive in the short-term (1–2 day) forecasts (e.g., Bowler et al. 2008), which is the time scale covered by the WAFS forecasts. To address this lack of spread, we use a multidiagnostic approach as a first attempt for probabilistic turbulence forecasts based on ensembles of the 15 CAT and 15 MWT diagnostics to develop a percentage agreement of exceeding a certain EDR threshold under the situation that the component CAT and MWT diagnostics are equally and randomly distributed in the model field regardless of their dependencies (see Fig. 4). In addition, given that turbulence in the free atmosphere occurs because of a combination of different generation mechanisms that are very hard to distinguish one by one independently from the nonlinear solution of the NWP model fields, the multidiagnostic ensemble gives better spread and takes into account possible uncertainties in the probabilistic turbulence forecast, although component diagnostics are not perfectly (ideally) independent to each other.

To do this, at each grid point, we simply count how many EDR-scaled turbulence diagnostics

exceed the EDR threshold of 0.22 $m^{2/3}$ s^{-1}, a value considered as moderate-or-greater (MOG) intensity of turbulence for midsize aircraft (Sharman et al. 2014). There are two reasons for using MOG instead of severe or greater (SOG). First, SOG turbulence is a very rare event, and there is an insufficient sample size for validation. Second, as turbulence observation, reporting, and forecast technologies have improved, aircraft are more likely to identify and avoid SOG areas, which makes it even more difficult to get samples of SOG events. A probabilistic EDR forecast is calculated separately for the CAT and MWT. Finally, the maximum gridpoint-by-gridpoint probability forecast between the CAT and MWT is considered as the final probabilistic EDR forecast.

Figure 7 shows a sample snapshot of the probabilistic EDR forecasts for CAT (upper), MWT (middle), and combined G-GTG (bottom) derived from the 18-h GFS forecast valid at 1800 UTC 6 January 2016. As seen in the deterministic G-GTG forecast in Fig. 6, the probabilistic G-GTG forecasts also have higher values across the North Atlantic Ocean, near northwestern Africa, and the southern tip of Greenland. For users, this probabilistic forecast product can be translated to a chance of encountering MOG-level en route turbulence because of the different generation mechanisms within a given grid box. For the future WAFS planned in Table 1, this method will be extended to take into account more reliable spreads of members of the NWP ensemble model outputs based on initial perturbations, different physical packages, stochastic methodologies, and multiple ensemble models (e.g., Bowler et al. 2008; Kim et al. 2015; Candille 2009; Park et al. 2008; Gill and Buchanan 2014).

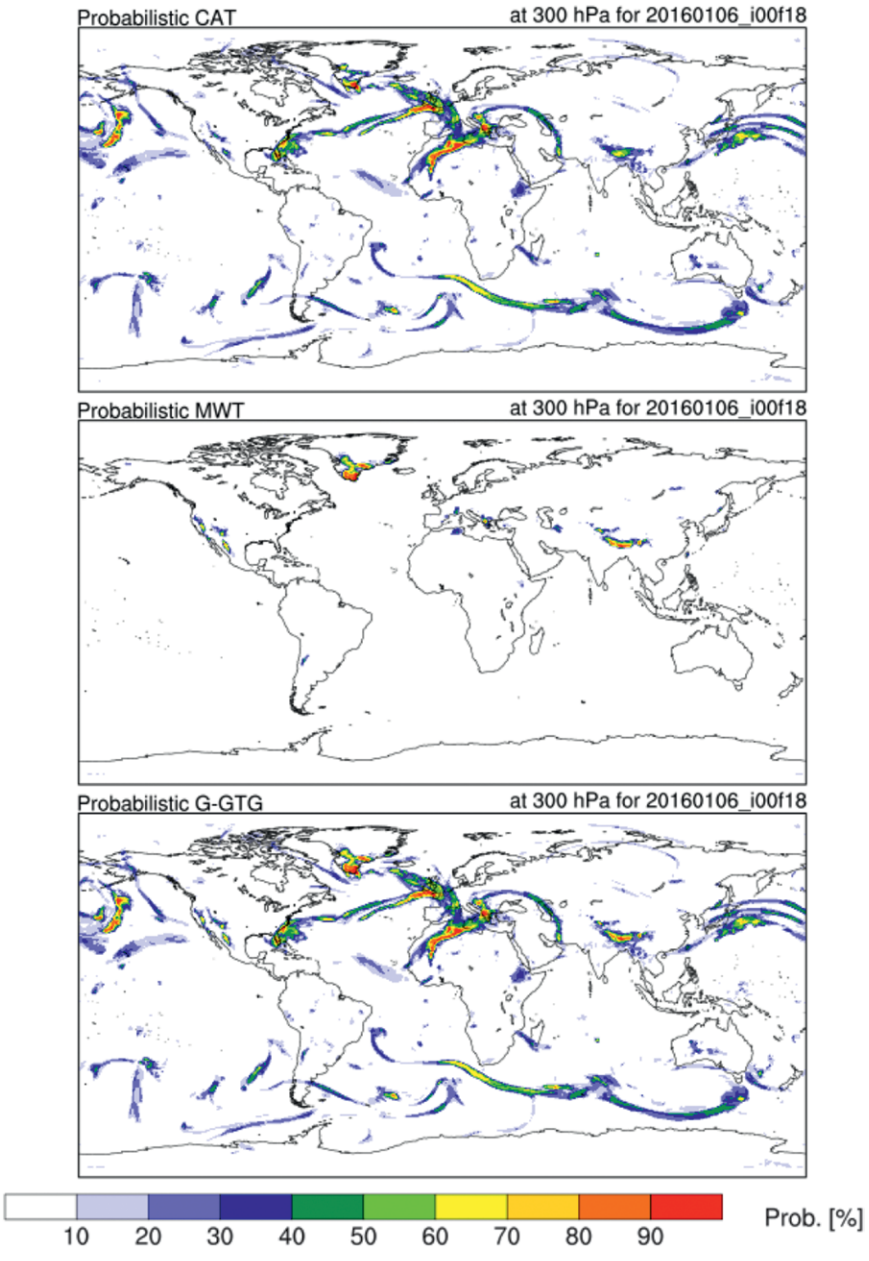

Fig. 7. As in Fig. 6, but for probabilistic (top) CAT, (middle) MWT, and (bottom) max G-GTG forecasts.

Blending of GFS-based G-GTG and UM-based G-GTG. For the operationally harmonized WAFS product between WAFC Washington and WAFC London, we apply the same GFS-based deterministic EDR-scale G-GTG system with the same diagnostic selection (appendix) to the Met Office's global UM on the same grid spacing as the GFS model. Figure 8 shows the deterministic EDR-scale CAT (left), MWT (center), and the maximum of CAT and MWT (right) forecasts from

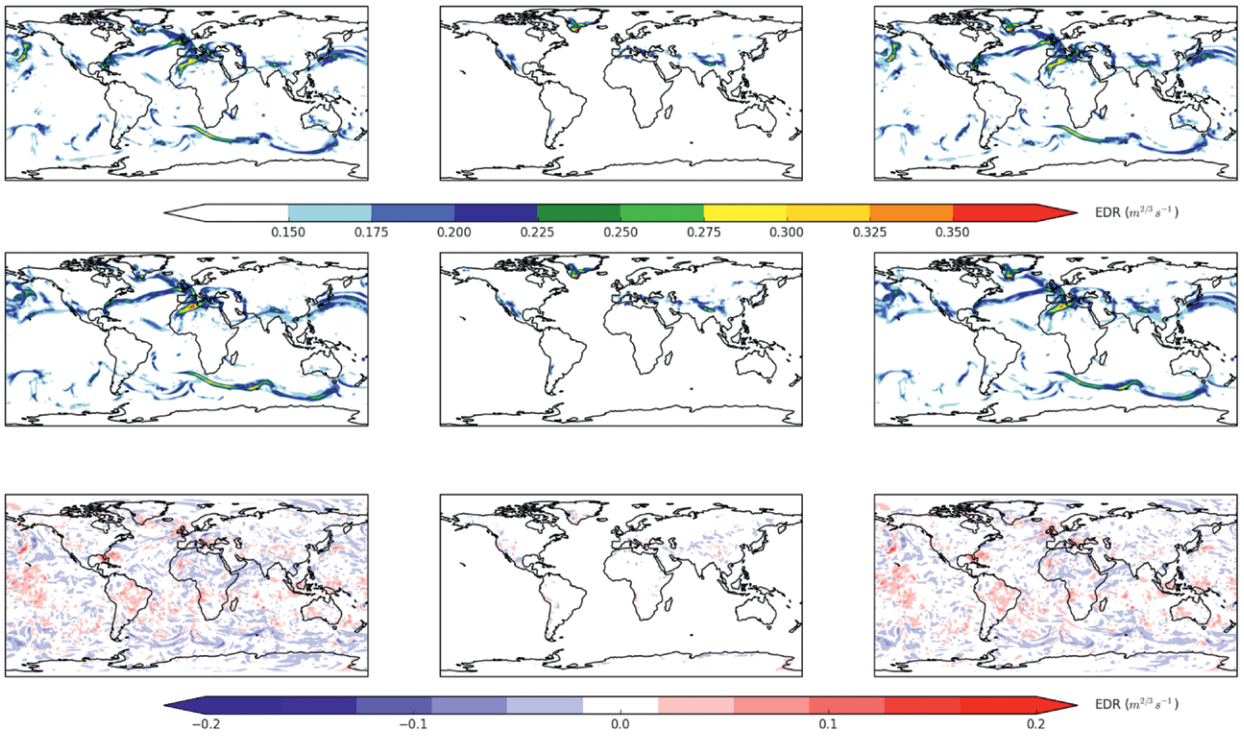

Fig. 8. A snapshot of the deterministic (left column) CAT, (middle column) MWT, and (right column) max G-GTG EDR forecasts from the same combination of 15 CAT and 15 MWT individual diagnostics (see appendix) at 300 hPa, derived from 18-h forecasts of the (top row) GFS and (middle row) UM, and (bottom row) their difference (GFS − UM) on 0.5° × 0.5° domain, both valid at 1800 UTC 6 Jan 2016.

the GFS (top) and the UM (middle). The differences between the GFS and UM (bottom) are also shown in Fig. 8, which shows only localized small discrepancies between these two models. In general, the two deterministic and probabilistic (not shown) EDR forecasts from the two different underlying NWP models have very similar patterns for this case, probably because the large-scale upper-level flows in both models have similar structures (not shown). Finally, in Fig. 9, EDR forecasts from both WAFC Washington (GFS based) and WAFC London (UM based) are blended by taking the maximum of the two deterministic (upper panel) and probabilistic (lower panel) EDR forecasts, which will give a consistent and harmonized en route turbulence forecast for the WAFS users all over the world.

Figure 10 shows a case study of the comparison of the current WAFS CAT product (left) with the final blended deterministic EDR (middle) and probabilistic EDR (right) forecasts, zoomed in on the North Atlantic flight corridor, which is one of the busiest flight corridors in the world. During this period, there are numerous MOG-level turbulence reports over southern Greenland. As shown in contours of sea level pressure (SLP) in Fig. 10, cyclonic flow associated with a low pressure system produces easterly winds at the surface over southern Greenland, generating a vertically propagating large-amplitude mountain wave, and a subsequent breakdown at the critical level at which there is a reversal of the background with height, from easterly to westerly. This is a frequent scenario for MWT as identified in climatology and case studies of turbulence over Greenland (e.g., Lane et al. 2009; Sharman et al. 2012a; Elvidge et al. 2017). This case as well as other cases under the similar synoptic pattern (not shown) are very well predicted by the blended deterministic and probabilistic G-GTG forecasts (middle and right panels), whereas the current WAFS forecast misses the MWT events over the southern tip of Greenland (left panel). In addition, the G-GTG forecast also captures some intermittent CIT or NCT along the surface front shown as a kink in SLP contours across the North Atlantic Ocean.

OBJECTIVE EVALUATIONS. *Global in situ EDR data.* Objective evaluations of both the deterministic and probabilistic G-GTG forecasts are conducted using in situ EDR data automatically recorded from selected aircraft with an onboard EDR estimation algorithm (Sharman et al. 2014; Cornman 2016). This provides location (latitude, longitude, and altitude), time, and intensities (1-min mean and peak EDR values) of each turbulence event that is either a regular (15-min

interval) or triggered event. Triggered events have three different types: 1) one 1-min peak EDR exceeds a 0.18 EDR value, 2) three of the last six 1-min peak EDRs exceed 0.12 EDR, and 3) the last six 1-min peak EDRs exceed 0.06 EDR. More detailed information about the in situ EDR reporting system can be found in Sharman et al. (2014). We compared G-GTG output with archived in situ EDR data within a ±1-h time window around 1800 UTC for the 6-month period October 2015–March 2016. This period was selected since this study is focused on evaluating nonconvective turbulence forecasts of CAT and MWT, which is climatologically more frequent in boreal winter periods in midlatitudes. We tried to avoid seasonal dependency by not using summer data that could have more CIT. Also, we tried to isolate a data period that was not influenced by upgrades of underlying NWP models. Figure 11 shows the horizontal distributions of the null (upper)- and MOG (lower)-level in situ EDR data used in this study. While most of the data are from the United States, there are also significant amounts of data across the Pacific and Atlantic Oceans corresponding to transoceanic long-haul flights from/to the United States to/from East Asia and Europe. These data are currently available for research purposes in archives at NCAR but are not publicly available because of airline proprietary issues.

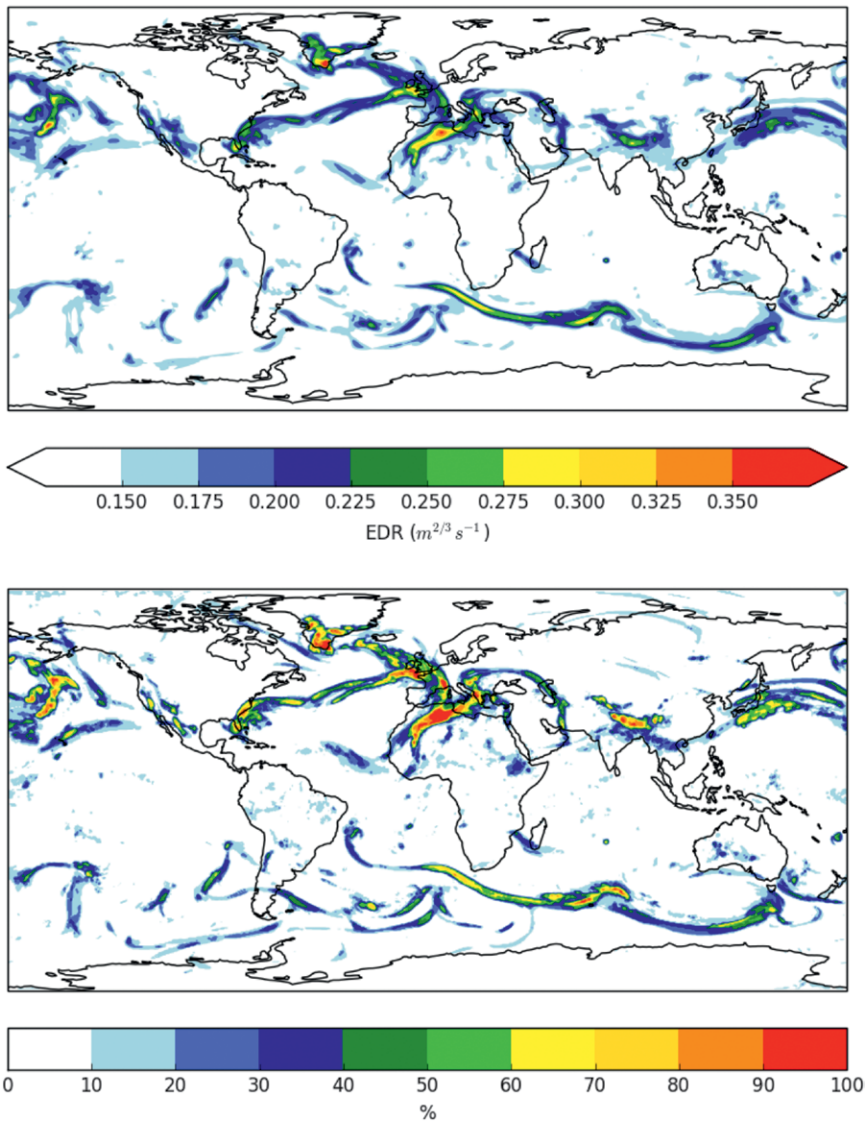

Fig. 9. A snapshot of the blended maximum EDR (top) deterministic and (bottom) probabilistic forecasts from the GFS-based G-GTG and UM-based G-GTG 18-h forecasts valid at 1800 UTC 6 Jan 2016.

Evaluation of deterministic EDR forecasts. For the evaluation of the deterministic EDR forecasts, the probability of detection (POD) "yes" for MOG-level turbulence events (EDR > 0.22 $m^{1/3}$ s^{-1}) and "no" for null turbulence events (EDR < 0.01 $m^{1/3}$ s^{-1}) are calculated by constructing the relative operating characteristics (ROC) curves as used in several previous studies (e.g., Sharman et al. 2006; Ellrod and Knox 2010; Kim et al. 2011; Gill 2014; Kim et al. 2015; Sharman and Pearson 2017). Figure 12 shows the resulting ROC curves with their area under curve (AUC) skill score (lower right) for the final deterministic GFS-based G-GTG EDR forecast (blue curve) and the single best CAT diagnostic (Ellrod3). For comparison, the current WAFS CAT product is also evaluated using the same in situ EDR data. The important message here is that the new G-GTG EDR forecast provides significant improvement over the current WAFS CAT product because of the incorporation of the improved diagnostics such as the Ellrod3 index, better resolution, and the inclusion of a specific MWT component as shown in Fig. 10.

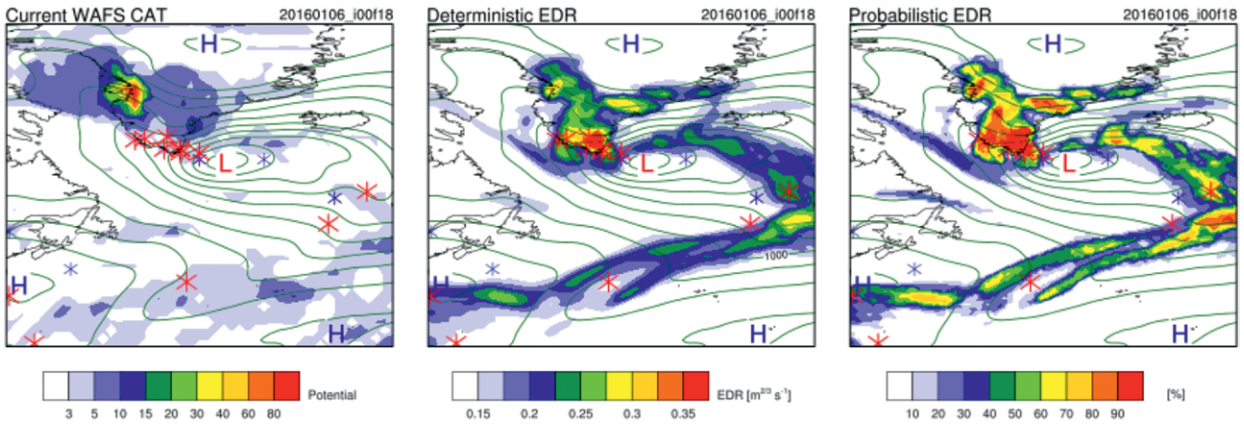

Fig. 10. A snapshot of the current (left) WAFS CAT potential, (middle) the blended maximum deterministic EDR, and (right) probabilistic EDR with SLP (contour with 8-hPa interval) from the GFS-based G-GTG and UM-based G-GTG valid at 1800 UTC 6 Jan 2016, focusing on the North Atlantic flight corridor. In situ PIREPs (MOG: red stars; null: blue stars) reported around ±1-h time window around this time is depicted.

Evaluation for probabilistic EDR forecast. To quantify the performance skill of the probabilistic G-GTG forecast, we also conducted the POD-based ROC curve using the same EDR data, showing the AUC skill score is 0.845 (not shown). Similar to the deterministic G-GTG (AUC = 0.85 in Fig. 12), the probabilistic G-GTG also outperforms the current WAFS as well as the best single CAT diagnostic (Ellrod3). In addition, the probabilistic G-GTG EDR forecast is evaluated using the reliability diagram (e.g., Gill and Buchanan 2014), which calculates the agreement of forecast probabilities with the actual occurrences in the same observed EDR data shown in Fig. 11. Figure 13 shows the reliability diagram for the GFS-based probabilistic G-GTG EDR forecasts for MOG (EDR > 0.22 $m^{1/3}$ s^{-1}; red line) and light-or-greater (LOG; EDR > 0.15 $m^{1/3}$ s^{-1}; blue line)-level turbulence. Here, the probability forecast can be translated into a chance of encountering a turbulent eddy due to the different CAT and MWT mechanisms in a given background condition in a gridbox area. The reliability line that is closest to the perfect line (diagonal solid black line) is considered a better probability forecast. In Fig. 13, as the EDR threshold for the probabilistic forecast increases from 0.15 (LOG) to 0.22 (MOG), fewer samples

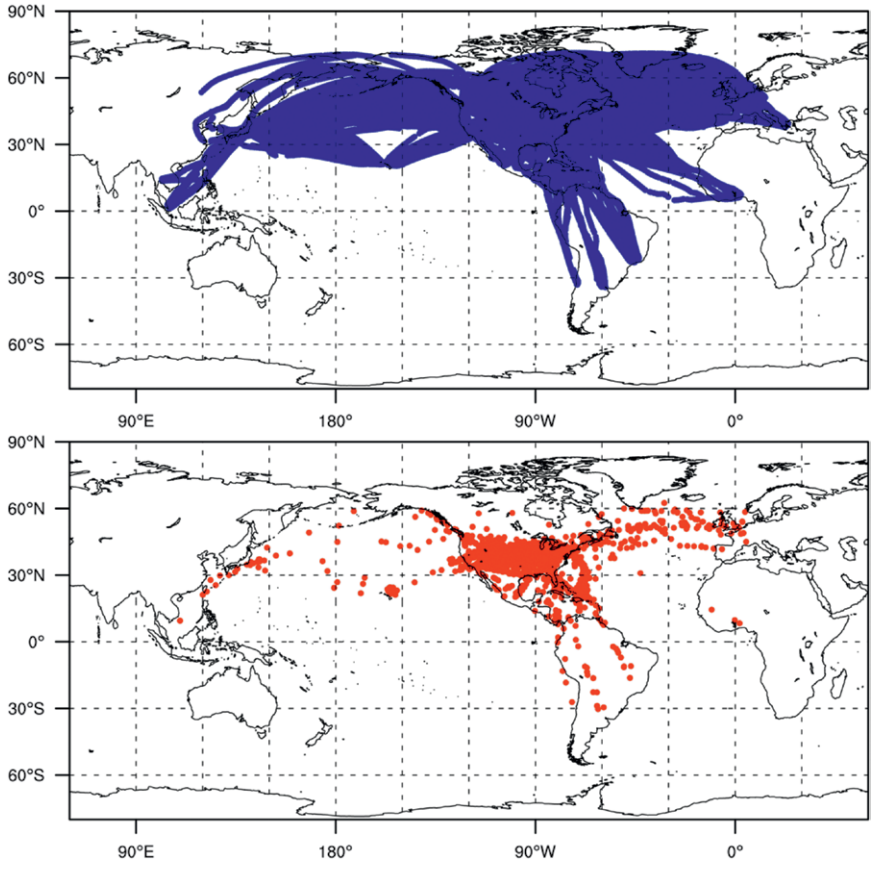

Fig. 11. Horizontal distributions of in situ EDR observations for (top) null EDR < 0.01 $m^{1/3}$ s^{-1} and for (bottom) MOG EDR > 0.22 $m^{1/3}$ s^{-1} measured by commercial aircraft for six months (Oct 2015–Mar 2016).

occur that correspond to the higher-probability forecasts (>75%), and this drops the reliability lines (red line) below the diagonal. In this study, the system is more reliable at predicting LOG-level turbulence than MOG level, which is likely due to the lack of observation data. The reliability line for the LOG level is still located to the right of the diagonal line, which implies that the probabilistic EDR forecasts are overforecasting. This could be because the ensemble of the 15 CAT and 15 MWT diagnostics from the underlying deterministic GFS model still does not provide enough spread in the probabilistic EDR forecasts. It is expected that better reliability and performance of the probabilistic EDR forecasts will be achieved by using more observation data and more spread of the NWP model ensembles with different initial perturbations, physical packages, stochastic methods, and multimodel solutions.

SUMMARY. For the next-generation version of the WAFS turbulence forecasts, we have developed the global Graphical Turbulence Guidance (G-GTG) applied to the global domain, which is based on the current operational GTG over the United States. The system captures multiple turbulence sources of CAT and MWT, derived from regions of high spatial gradients of meteorological variables based on theoretical and empirical turbulence generation mechanisms from two different underlying NWP models. Using a statistical EDR conversion methodology, raw values of the individual turbulence diagnostics are converted into the EDR to 1/3 power, consistent with the ICAO standard for turbulence reporting. A deterministic "ensemble mean" EDR forecast is provided by combining EDR-scaled CAT and MWT component diagnostics. We also produced a probabilistic EDR forecast from the multidiagnostic ensemble method by counting the number of the 15 CAT and 15 MWT diagnostics that exceed a certain EDR threshold. Those were shown to provide considerably superior statistical performance than the current WAFS CAT and also to provide better performance than the best single turbulence diagnostic when verified against a 6-month period of global in situ EDR observation data. Reliability tests of the probabilistic EDR forecast against the same in situ EDR data showed that the system is more reliable at predicting LOG turbulence (i.e., EDR > 0.15 $m^{2/3}$ s^{-1}) than MOG turbulence (i.e., EDR > 0.22 $m^{2/3}$ s^{-1}) in this study, although it suffers from overforecasting. It is likely to be related to the lack of observation data and global NWP ensemble spread in short-term (18 h) forecast.

The global GTG system developed for the WAFS will be beneficial for global flight

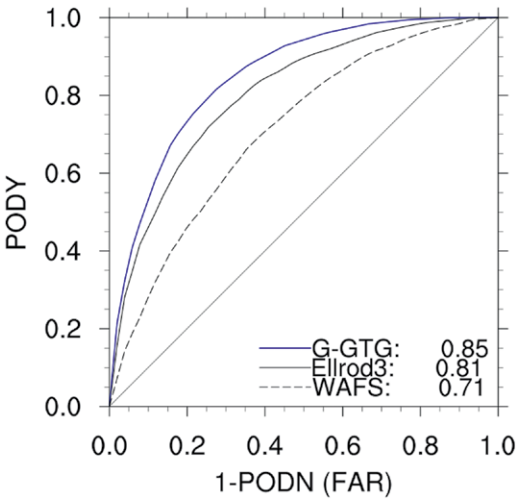

Fig. 12. Statistical performance as indicated by ROC curves for the deterministic G-GTG EDR forecast (solid blue curve) and the single best CAT diagnostic (Ellrod3; solid black curve) with the AUC skill scores (lower right), derived from 6-month period (Oct 2015–Mar 2016) of 18-h GFS forecast data. The statistics are based on the POD "yes" for MOG turbulence (EDR > 0.22 $m^{1/3}$ s^{-1}) and "no" for null turbulence (EDR < 0.01 $m^{1/3}$ s^{-1}) observation data shown in Fig. 11. For direct comparison, current WAFS CAT product (dashed black curve) is also evaluated using the same data.

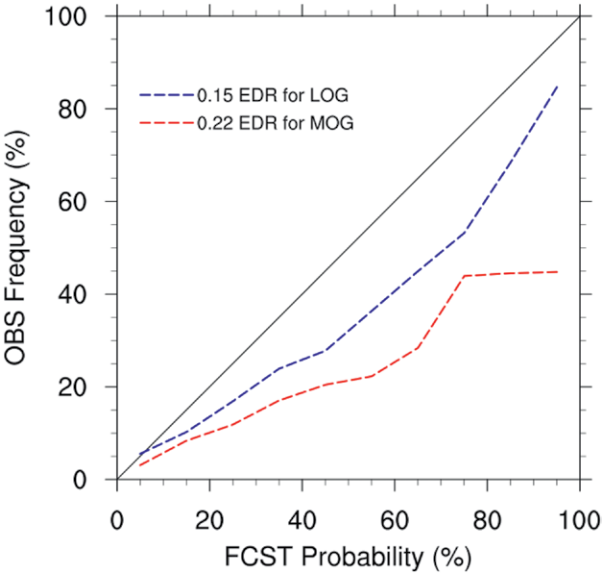

Fig. 13. Statistical reliability lines (dashed colored lines) for the probabilistic G-GTG EDR forecasts for MOG (EDR > 0.22 $m^{1/3}$ s^{-1}; red line)- and LOG (EDR > 0.15 $m^{1/3}$ s^{-1}; blue line)-level turbulence using 6-month period of 18-h GFS forecast data and in situ EDR observation data shown in Fig. 11. The perfect reliability line (black solid diagonal line) is also depicted in the plot.

planning by international aviation users. The WAFC Washington (NOAA/Aviation Weather Center) and WAFC London (Met Office) will continue to develop and implement upgrades to meet the requirements set forth in the ICAO's Aviation System Block Upgrade (ASBU) (Table 1). To achieve those goals, there are still several challenges to be resolved in the future, as follows:

1) Better understanding of the turbulence downscaling process from resolved large scales to smaller scales is necessary. New diagnostics or better subgrid-scale (SGS) turbulence parameterizations appropriate for stably stratified shear flow in the UTLS could be developed using observation campaigns and multinested high-resolution numerical simulations (e.g., Sharman and Lane 2016).
2) As turbulence forecasting depends highly upon underlying NWP model configurations, such as initial and boundary conditions, data assimilation, and physical parameterizations, the downstream impact to turbulence forecasts from changes to the underlying NWP must be identified and the G-GTG configuration modified for the best performance (e.g., Park et al. 2016).
3) Obtaining more observational data, especially in poorly observed regions like the Southern Hemisphere, is necessary. Data-quality-controlled automated onboard in situ turbulence data covering more areas of the world are important not only for increased situational awareness but also for more reliable evaluation opportunities for the NWP model–based EDR forecast products.
4) The probabilistic EDR forecasts described in this study suffer from overforecasting turbulence (Fig. 13), mainly due to a lack of observation data and realistic ensemble spread. Therefore, it will be necessary to use a combination of multiple ensemble systems that feature a variety of perturbations [initial perturbations, various physical packages and parameters (stochastic method), and multidynamic cores] in order to achieve a more reliable spread. And it will be also be required to develop appropriate training tools and materials to give better insights to understanding probabilistic forecast information to users.

ACKNOWLEDGMENTS. This research is in response to the requirements and funding by the Federal Aviation Administration (FAA; Grant DTFACT-17-X-80002). The views expressed in this work are those of the authors and do not necessarily represent the official policy or position of the FAA. JHK (Jung-Hoon Kim) was recently supported by Research Resettlement Fund for the new faculty of Seoul National University.

APPENDIX: DETAILED INFORMATION FOR INDIVIDUAL TURBULENCE DIAGNOSTICS.

Here, we list the 15 CAT and 15 MWT diagnostics used in the G-GTG evaluations. See Sharman and Pearson (2017) and the cited references for more complete descriptions.

15 CAT diagnostics.

1) Ellrod3 (s^{-2}): (vertical wind shear × total deformation) + divergence tendency (Ellrod and Knox 2010)
2) Fth/Ri ($m^2\ s^{-3}$): normalized 2D frontogenesis function on isentropic surfaces divided by the gradient Richardson number (Sharman and Pearson 2017)
3) NGM1 ($m\ s^{-2}$): wind speed × total deformation (Reap 1996)
4) DEFSQ (s^{-2}): the square of total deformation (Sharman et al. 2006)
5) |DIV|/Ri (s^{-1}): absolute value of horizontal divergence divided by the gradient Richardson number (Sharman and Pearson 2017)
6) IAWIND ($m\ s^{-2}$): inertial advective wind (McCann 2011)
7) UBF/Ri (s^{-2}): unbalanced flow divided by the gradient Richardson number (Koch and Caracena 2002)
8) EDRAVG ($m^{4/3}\ s^{-2}$): $e^{2/3}$ estimated from the average of longitudinal and transverse second-order structure functions for horizontal wind components (Frehlich and Sharman 2004a)
9) EDRLL ($m^{4/3}\ s^{-2}$): $e^{2/3}$ estimated from the second-order longitudinal structure function for zonal wind component (Frehlich and Sharman 2004a)
10) |TEMPG|/Ri ($K\ m^{-1}$): absolute value of horizontal temperature gradient divided by the gradient Richardson number (Sharman and Pearson 2017)
11) NCSU2/Ri (s^{-3}): |vertical vorticity gradient × gradient of Montgomery streamfunction| divided by the gradient Richardson number (Kaplan et al. 2004)
12) EDRLUN ($m^{2/3}\ s^{-1}$): $e^{1/3}$ estimated from simplified $D\mathrm{Ri}/Dt$ (Gill and Buchanan 2014)
13) WSQ/Ri ($m^2\ s^{-2}$): the square of vertical velocity divided by the gradient Richardson number (Sharman and Pearson 2017)
14) SIGWAVG/Ri ($m^2\ s^{-2}$): variance of vertical velocity estimated from average of longitudinal and latitudinal second-order structure function divided by the gradient Richardson number (Frehlich and Sharman 2004b)
15) RTKE ($m^2\ s^{-2}$): resolved turbulent kinetic energy (Stull 1998)

Note that some of these CAT diagnostics are normalized by the local gradient Richardson number (Ri), which has been found to provide better statistical performance against the observation data (e.g., Kim et al. 2015; Sharman and Pearson 2017).

15 MWT diagnostics. The mws = gridpoint height (m) × horizontal gradient of the height (m km^{-1}). This is to isolate geographic regions of likely MWT and to represent topographic forcing [see Sharman and Pearson (2017) for details].

1) MWT1 (m^3 s^{-3}): mws × WSQ/Ri
2) MWT2 (K^2 m$^{1/3}$ s^{-1}): mws × CTSQ (temperature structure constant estimated from zonal and meridional structure functions of *T*; Frehlich and Sharman 2010)
3) MWT3 (m^2 s^{-2}): mws × F3D (3D frontogenesis function on constant *z* surfaces; Sharman and Pearson 2017)
4) MWT4 (m^2 s^{-2}): mws × horizontal wind speed
5) MWT5 (m s^{-2}): mws × |DIV|
6) MWT6 (m s^{-2}): mws × NGM1
7) MWT7 (m^3 s^{-3}): mws × SIGWAVG
8) MWT8 (m^2 s^{-1}): mws × LHFK/Ri (Lighthill–Ford radiation term divided by local Richardson number; Knox et al. 2008)
9) MWT9 (m^3 s^{-2}): mws × IAWIND
10) MWT10 (m$^{7/3}$ s^{-3}): mws × EDRAVG
11) MWT11 (m$^{5/3}$ s^{-2}): mws × SCHGW ($e^{1/3}$ derived from variance of vertical velocity; Schumann 2012)
12) MWT12 (K s^{-1}): mws × |TEMPG|
13) MWT13 (m s^{-2}): mws × DEFSQ
14) MWT14 (m$^{7/3}$ s^{-3}): mws × EDRLL
15) TKE_GWB (N m^{-2}): the single-column model-based orographic gravity wave drag (Palmer et al. 1986)

REFERENCES

Bowler, N. E., A. Alberto, K. R. Mylne, K. B. Robertson, and S. E. Beare, 2008: The MOGREPS short-range ensemble prediction system. *Quart. J. Roy. Meteor. Soc.*, **134**, 703–722, https://doi.org/10.1002/qj.234.

Buizza, R., A. Hollingsworth, F. Lalaurette, and A. Ghelli, 1999: Probabilistic predictions of precipitation using the ECMWF ensemble prediction system. *Wea. Forecasting*, **14**, 168–189, https://doi.org/10.1175/1520-0434(1999)014<0168:PPOPUT>2.0.CO;2.

Candille, G., 2009: The multiensemble approach: The NAEFS example. *Mon. Wea. Rev.*, **137**, 1655–1665, https://doi.org/10.1175/2008MWR2682.1.

Cho, J. Y. N., and E. Lindborg, 2001: Horizontal velocity structure functions in the upper troposphere and lower stratosphere: 1. Observations. *J. Geophys. Res.*, **106**, 10 223–10 232, https://doi.org/10.1029/2000JD900814.

Civil Air Navigation Services Organization, 2014: Introduction to the Aviation System Block Upgrade (ASBU) modules—Strategic planning for ASBU modules implementation. Civil Air Navigation Services Organization Doc. 000111222333XYZ, 45 pp.

Clark, T. L., and W. R. Peltier, 1984: Critical level reflection and the resonant growth of nonlinear mountain waves. *J. Atmos. Sci.*, **41**, 3122–3134, https://doi.org/10.1175/1520-0469(1984)041<3122:CLRATR>2.0.CO;2.

——, W. D. Hall, R. M. Kerr, D. Middleton, L. Radke, F. M. Ralph, P. J. Nieman, and D. Levinson, 2000: Origins of aircraft-damaging clear-air turbulence during the 9 December 1992 Colorado downslope windstorm: Numerical simulations and comparison with observations. *J. Atmos. Sci.*, **57**, 1105–1131, https://doi.org/10.1175/1520-0469(2000)057<1105:OOADCA>2.0.CO;2.

Cornman, L. B., 2016: Airborne in situ measurements of turbulence. *Aviation Turbulence: Processes, Detection, Prediction*, R. Sharman and T. Lane, Eds., Springer, 97–120, https://doi.org/10.1007/978-3-319-23630-8_5.

Doyle, J. D., M. A. Shapiro, Q. Jiang, and D. L. Bartels, 2005: Large-amplitude mountain wave breaking over Greenland. *J. Atmos. Sci.*, **62**, 3106–3126, https://doi.org/10.1175/JAS3528.1.

Dutton, J. A., and H. A. Panofsky, 1970: Clear air turbulence: A mystery may be unfolding. *Science*, **167**, 937–944, https://doi.org/10.1126/science.167.3920.937.

Ellrod, G. P., and D. I. Knapp, 1992: An objective clear-air turbulence forecasting technique: Verification and operational use. *Wea. Forecasting*, **7**, 150–165, https://doi.org/10.1175/1520-0434(1992)007<0150:AOCATF>2.0.CO;2.

——, and J. A. Knox, 2010: Improvements to an operational clear-air turbulence diagnostic index by addition of a divergence trend term. *Wea. Forecasting*, **25**, 789–798, https://doi.org/10.1175/2009WAF2222290.1.

Elvidge, A. D., S. B. Vosper, H. Wells, J. C. H. Cheung, S. H. Derbyshire, and D. Turp, 2017: Moving towards a wave-resolved approach to forecasting mountain wave induced clear air turbulence. *Meteor. Appl.*, **24**, 540–550, https://doi.org/10.1002/met.1656.

Frehlich, R., and R. Sharman, 2004a: Estimates of turbulence from numerical weather prediction model output with applications to turbulence diagnosis and data assimilation. *Mon. Wea. Rev.*, **132**, 2308–2324, https://doi.org/10.1175/1520-0493(2004)132<2308:EOTFNW>2.0.CO;2.

——, and ——, 2004b: Estimates of upper level turbulence based on second order structure functions derived from numerical weather prediction model output. *11th Conf. on Aviation, Range, and Aerospace Meteorology*, Hyannis, MA, Amer. Meteor. Soc., 4.13, https://ams.confex.com/ams/11aram22sls/techprogram/paper_81831.htm.

——, and ——, 2010: Climatology of velocity and temperature turbulence statistics determined from rawinsonde and ACARS/AMDAR data. *J. Appl. Meteor. Climatol.*, **49**, 1149–1169, https://doi.org/10.1175/2010JAMC2196.1.

Gill, P. G., 2014: Objective verification of World Area Forecast Centre clear air turbulence forecasts. *Meteor. Appl.*, **21**, 3–11, https://doi.org/10.1002/met.1288.

——, and P. Buchanan, 2014: An ensemble based turbulence forecasting system. *Meteor. Appl.*, **21**, 12–19, https://doi.org/10.1002/met.1373.

ICAO, 2001: Meteorological service for international air navigation. 14th ed. ICAO Rep., 128 pp.

——, 2012: Guidance on the harmonized WAFS grids for cumulonimbus cloud, icing and turbulence forecasts: Version 2.5. Met Office and NOAA Rep., 14 pp.

Kaplan, M. L., and Coauthors, 2004: Characterizing the severe turbulence environments associated with commercial aviation accidents: A real-time turbulence model (RTTM) designed for the operational prediction of hazardous aviation turbulence environments. NASA Rep. NASA/CR-2004-213025, 54 pp., https://ntrs.nasa.gov/archive/nasa/casi.ntrs.nasa.gov/20040110976.pdf.

Koch, S. E., and F. Caracena, 2002: Predicting clear-air turbulence from diagnosis of unbalance flow. Preprints, *10th Conf. on Aviation, Range, and Aerospace Meteorology*, Portland, OR, Amer. Meteor. Soc., 359–363.

Jaeger, E. B., and M. Sprenger, 2007: A Northern Hemispheric climatology of indices for clear air turbulence in the tropopause region derived from ERA40 reanalysis data. *J. Geophys. Res.*, **112**, D20106, https://doi.org/10.1029/2006JD008189.

Kim, J.-H., and H.-Y. Chun, 2010: A numerical study of clear-air turbulence (CAT) encounters over South Korea on 2 April 2007. *J. Appl. Meteor. Climatol.*, **49**, 2381–2403, https://doi.org/10.1175/2010JAMC2449.1.

——, and ——, 2011: Statistics and possible sources of aviation turbulence over South Korea. *J. Appl. Meteor. Climatol.*, **50**, 311–324, https://doi.org/10.1175/2010JAMC2492.1.

——, and ——, 2012: A numerical simulation of convectively induced turbulence above deep convection. *J. Appl. Meteor. Climatol.*, **51**, 1180–1200, https://doi.org/10.1175/JAMC-D-11-0140.1.

——, ——, R. D. Sharman, and T. L. Keller, 2011: Evaluations of upper-level turbulence diagnostics performance using the Graphical Turbulence Guidance (GTG) system and pilot reports (PIREPs) over East Asia. *J. Appl. Meteor. Climatol.*, **50**, 1936–1951, https://doi.org/10.1175/JAMC-D-10-05017.1.

——, ——, ——, and S. B. Trier, 2014: The role of vertical shear on aviation turbulence within cirrus bands of a simulated western Pacific cyclone. *Mon. Wea. Rev.*, **142**, 2794–2813, https://doi.org/10.1175/MWR-D-14-00008.1.

——, W. N. Chan, B. Sridhar, and R. D. Sharman, 2015: Combined winds and turbulence prediction system for automated air-traffic management applications. *J. Appl. Meteor. Climatol.*, **54**, 766–784, https://doi.org/10.1175/JAMC-D-14-0216.1.

Kim, S.-H., and H.-Y. Chun, 2016: Aviation turbulence encounters detected from aircraft observations: Spatiotemporal characteristics and application to Korean Aviation Turbulence Guidance. *Meteor. Appl.*, **23**, 594–604, https://doi.org/10.1002/met.1581.

Knox, J. A., 1997: Possible mechanisms of clear-air turbulence in strongly anticyclonic flow. *Mon. Wea. Rev.*, **125**, 1251–1259, https://doi.org/10.1175/1520-0493(1997)125<1251:PMOCAT>2.0.CO;2.

——, D. W. McCann, and P. D. Williams, 2008: Application of the Lighthill–Ford theory of spontaneous imbalance to clear-air turbulence forecasting. *J. Atmos. Sci.*, **65**, 3292–3304, https://doi.org/10.1175/2008JAS2477.1.

Koch, S. E., and Coauthors, 2005: Turbulence and gravity waves within an upper-level front. *J. Atmos. Sci.*, **62**, 3885–3908, https://doi.org/10.1175/JAS3574.1.

Lane, T. P., 2016: Processes underlying near-cloud turbulence. *Aviation Turbulence: Processes, Detection, Prediction*, R. Sharman and T. Lane, Eds., Springer, 97–120, https://doi.org/10.1007/978-3-319-23630-8_16.

——, and R. D. Sharman, 2006: Gravity wave breaking, secondary wave generation, and mixing above deep convection in a three-dimensional cloud model. *Geophys. Res. Lett.*, **33**, L23813, https://doi.org/10.1029/2006GL027988.

——, J. D. Doyle, R. Plougonven, M. A. Shapiro, and R. D. Sharman, 2004: Observations and numerical simulations of inertia–gravity waves and shearing instabilities in the vicinity of a jet stream. *J. Atmos. Sci.*, **61**, 2692–2706, https://doi.org/10.1175/JAS3305.1.

——, ——, R. D. Sharman, M. A. Shapiro, and C. D. Watson, 2009: Statistics and dynamics of aircraft encounters of turbulence over Greenland. *Mon. Wea. Rev.*, **137**, 2687–2702, https://doi.org/10.1175/2009MWR2878.1.

——, R. D. Sharman, S. B. Trier, R. G. Fovell, and J. K. Williams, 2012: Recent advances in the understanding

of near-cloud turbulence. *Bull. Amer. Meteor. Soc.*, **93**, 499–515, https://doi.org/10.1175/BAMS-D-11-00062.1.

Lester, P. F., 1994: *Turbulence: A New Perspective for Pilots*. Jeppesen Sanderson, 212 pp.

Lilly, D. K., 1978: A severe downslope windstorm and aircraft turbulence event induced by a mountain wave. *J. Atmos. Sci.*, **35**, 59–77, https://doi.org/10.1175/1520-0469(1978)035<0059:ASDWAA>2.0.CO;2.

McCann, D. W., 2001: Gravity waves, unbalanced flow, and aircraft clear air turbulence. *Natl. Wea. Dig.*, **25** (1–2), 3–14, http://nwafiles.nwas.org/digest/papers/2001/Vol25No12/Pg3-McCann.pdf.

Nastrom, G. D., and K. S. Gage, 1985: A climatology of atmospheric wavenumber spectra of wind and temperature observed by commercial aircraft. *J. Atmos. Sci.*, **42**, 950–960, https://doi.org/10.1175/1520-0469(1985)042<0950:ACOAWS>2.0.CO;2.

Palmer, T. N., G. J. Shutts, and R. Swinbank, 1986: Alleviation of a systematic westerly bias in general circulation and numerical weather prediction models through an orographic gravity wave drag parametrization. *Quart. J. Roy. Meteor. Soc.*, **112**, 1001–1039, https://doi.org/10.1002/qj.49711247406.

Park, S.-H., J.-H. Kim, R. D. Sharman, and J. B. Klemp, 2016: Update of upper-level turbulence forecast by reducing unphysical components of topography in the numerical weather prediction model. *Geophys. Res. Lett.*, **43**, 7718–7724, https://doi.org/10.1002/2016GL069446.

Park, Y.-Y., R. Buizza, and M. Leutbecher, 2008: TIGGE: Preliminary results on comparing and combining ensembles. *Quart. J. Roy. Meteor. Soc.*, **134**, 2029–2050, https://doi.org/10.1002/qj.334.

Reap, R. M., 1996: Probability forecasts of clear-air-turbulence for the contiguous U.S. National Weather Service Office of Meteorology Tech. Procedures Bull. Rep. 430, 15 pp.

Schumann, U., 2012: A contrail cirrus prediction model. *Geosci. Model Dev.*, **5**, 543–580, https://doi.org/10.5194/gmd-5-543-2012.

Sela, J., 2010: The derivation of sigma-pressure hybrid coordinate semi-Lagrangian model equations for the GFS. NCEP Office Note 462, 31 pp.

Sharman, R., and T. Lane, Eds., 2016: *Aviation Turbulence: Processes, Detection, Prediction*. Springer, 523 pp., https://doi.org/10.1007/978-3-319-23630-8.

——, and J. Pearson, 2017: Prediction of energy dissipation rates for aviation turbulence. Part I: Forecasting nonconvective turbulence. *J. Appl. Meteor. Climatol.*, **56**, 317–337, https://doi.org/10.1175/JAMC-D-16-0205.1.

——, C. Tebaldi, G. Wiener, and J. Wolff, 2006: An integrated approach to mid- and upper-level turbulence forecasting. *Wea. Forecasting*, **21**, 268–287, https://doi.org/10.1175/WAF924.1.

——, J. D. Doyle, and M. A. Shapiro, 2012a: An investigation of a commercial aircraft encounter with severe clear-air turbulence over western Greenland. *J. Appl. Meteor. Climatol.*, **51**, 42–53, https://doi.org/10.1175/JAMC-D-11-044.1.

——, S. B. Trier, T. P. Lane, and J. D. Doyle, 2012b: Sources and dynamics of turbulence in the upper troposphere and lower stratosphere: A review. *Geophys. Res. Lett.*, **39**, L12803, https://doi.org/10.1029/2012GL051996.

——, L. B. Cornman, G. Meymaris, J. Pearson, and T. Farrar, 2014: Description and derived climatologies of automated in situ eddy-dissipation-rate reports of atmospheric turbulence. *J. Appl. Meteor. Climatol.*, **53**, 1416–1432, https://doi.org/10.1175/JAMC-D-13-0329.1.

Storer, L. N., P. D. Williams, and M. M. Joshi, 2017: Global response of clear-air turbulence to climate change. *Geophys. Res. Lett.*, **44**, 9976–9984, https://doi.org/10.1002/2017GL074618.

Stull, R. B., 1988: *An Introduction to Boundary Layer Meteorology*. Kluwer Academic, 670 pp.

Walters, D., and Coauthors, 2017: The Met Office Unified Model Global Atmosphere 6.0/6.1 and JULES Global Land 6.0/6.1 configurations. *Geosci. Model Dev.*, **10**, 1487–1520, https://doi.org/10.5194/gmd-10-1487-2017.

Williams, P. D., 2017: Increased light, moderate, and severe clear-air turbulence in response to climate change. *Adv. Atmos. Sci.*, **34**, 576–586, https://doi.org/10.1007/s00376-017-6268-2.

——, and M. M. Joshi, 2013: Intensification of winter transatlantic aviation turbulence in response to climate change. *Nat. Climate Change*, **3**, 644–648, https://doi.org/10.1038/nclimate1866.

WMO–ICAO, 2014: Met divisional meeting—Initial draft roadmap for the World Area Forecast System (WAFS). WMO–ICAO Rep. MET/14-IP2 CAeM-15/INF.2 17/1/14, 16 pp.

Wolff, J. K., and R. D. Sharman, 2008: Climatology of upper-level turbulence over the contiguous United States. *J. Appl. Meteor. Climatol.*, **47**, 2198–2214, https://doi.org/10.1175/2008JAMC1799.1.

Zhang, F., 2004: Generation of mesoscale gravity waves in upper-tropospheric jet–front systems. *J. Atmos. Sci.*, **61**, 440–457, https://doi.org/10.1175/1520-0469(2004)061<0440:GOMGWI>2.0.CO;2.

AMS Members

Give a great gift at a great price

Looking for the perfect present for the weather enthusiast in your life? Want to make a valuable contribution to your local library or community college?

Send a subscription to Weatherwise magazine for just $24.95*—That's nearly 50% off the list price!

Contact Member Services by e-mail at **amsmem@ametsoc.org** or by phone at **617-227-2425** to place all of your Weatherwise orders today!

Written for a general audience, Weatherwise offers a colorful and nontechnical look at recent discoveries in meteorology and climatology.

Check out the latest table of contents at www.weatherwise.org.

Want your own?
Then order a personal subscription at the same great price.

*Cost for delivery outside of the U.S. is $40.95. Weatherwise is available to AMS Members through a cooperative agreement with Taylor & Francis Group LLC, the publishers of Weatherwise.